© 2011 Alexander D. Pawlicki

THREE-DIMENSIONAL IMPEDANCE MAP ANALYSIS OF BIOLOGICAL TISSUE TO ELUCIDATE SMALL-SCALE ACOUSTIC SCATTERING BEHAVIOR

BY

ALEXANDER D. PAWLICKI

THESIS

Submitted in partial fulfillment of the requirements
for the degree of Master of Science in Electrical and Computer Engineering
in the Graduate College of the
University of Illinois at Urbana-Champaign, 2011

Urbana, Illinois

Adviser:

Professor William D. O'Brien, Jr.

Abstract

Three-dimensional impedance maps (3DZMs) are computational models of acoustic impedance of tissue constructed from a series of adjacent histology images. The power spectrum of a 3DZM can be analyzed to estimate model-based quantitative ultrasound parameters such as effective scatterer diameter (ESD) and effective acoustic concentration (EAC). The goal in this approach is to determine a link between the quantitative ultrasound estimates made from tissue and actual tissue structures seen in histology as a means of identifying the ultrasonic scattering sites in different types of tissue.

The 3DZM construction and analysis routines have been updated in order to increase speed and overall performance. In particular, the map creation algorithm was structured in a parallel implementation to greatly increase speed. The ESD analysis algorithm was modified to increase both speed and accuracy, and an EAC estimator has been implemented also. The new analysis algorithm was tested through simulating 3DZMs and was found to be very accurate for estimating ESD, but only accurate up to an offset for EAC.

The 3DZM method was then applied to rabbit liver and rat cervix tissue. ESD estimates for both normal and fatty rabbit liver were made with average values of 7.5 ± 1.3 μm and 7.0 ± 0.3 μm, respectively. This size was identified to be very near that of a cell nucleus. ESD estimates of the rat cervix tissue had an average value of 11.3 ± 3.1 μm. This size did not correspond to any readily apparent structures in the tissue but fell within the range of estimates made from real ultrasound data.

This work seeks to evaluate and improve upon the previous work of the 3DZM method.

Acknowledgments

This work was made possible by the contributions of many individuals. Firstly I would like to thank my adviser Dr. William D. O'Brien, Jr. I would also like to thank the members of the Bioacoustics Research Lab, specifically the contributions of Dr. Michael L. Oelze, Veterinarian Rita J. Miller, and Dr. Barbara L. McFarlin. Finally, I recognize the support of my parents Anne and Peter, and my brothers Patrick and Matthew. This work was funded by NIH Grant R01CA111289.

Table of Contents

Chapter 1: Introduction

Ultrasound imaging is safe, portable and inexpensive when compared to other imaging modalities such as X-ray, computed tomography, and magnetic resonance imaging [1]. These advantages make ultrasound an active area of research to expand the capabilities and diagnostic function of medical ultrasound. Conventional B-mode imaging provides a mainly qualitative description of tissue macrostructure and contains only part of the information available in the echo signal. Quantitative ultrasound (QUS) seeks to utilize frequency-dependent details available from radio-frequency (RF) echo signals to make a quantitative assessment of tissue microstructure.

The success of QUS techniques depends on the development and use of accurate scattering models for tissue microstructure. The three-dimensional impedance map (3DZM) method [2] has been developed as a means of better understanding the scattering of tissue microstructure. 3DZMs are computational models of acoustic impedance and are a powerful tool in studying small-scale acoustic scattering in biological tissue. They provide a means of connecting ultrasonic and histological characterization of tissue.

Chapter 2 provides an overview of the theory that allows 3DZMs to be related to ultrasonic backscatter. Chapter 3 describes in detail the method in which a 3DZM is constructed. Chapter 4 describes the analysis of 3DZMs for estimating QUS parameters. Chapter 5 presents the results of analysis done on simulated 3DZMs. Chapter 6 presents the results when the 3DZM method was applied to rabbit liver and rat cervix. Chapter 7 contains conclusions, a summary of contributions so far, and plans for future work.

1.1 Quantitative Ultrasound

A typical ultrasound image is created first by receiving the backscattered radio frequency (RF) signal of an ultrasound pulse, which is the result of scattering from tissue boundaries, structures, etc. The envelope of the received signal is computed by taking the Hilbert transform and the result is log-compressed to form a conventional B-mode image. By computing the envelope of the signal, much of the frequency-dependent information contained in the signal is lost.

QUS seeks to utilize this frequency dependent information of the RF signal in order to gain a quantitative description of the properties of tissue microstructure. Several QUS parameters can be deduced from the backscatter coefficient, the fundamental quantity describing the frequency dependence of backscattered ultrasound from a scattering volume. Two such parameters are the effective scatterer diameter (ESD) and the effective acoustic concentration (EAC). Estimates of these two parameters provide information about the approximate scatterer size of tissue microstructures (ESD), as well as a coupled measure of the concentration and strength of scattering sites (EAC). Quantitative ultrasound parameters have previously been shown to be a means of enhancing the capabilities of ultrasound imaging [3], and have been able to provide quantitative information about liver, renal, cervical, and many other types of tissue [4, 5, 6]. However, improving the results of QUS requires a more detailed understanding of the interaction between ultrasound and tissue microstructure.

1.2 Three-Dimensional Impedance Maps

Three-dimensional impedance maps are computational models of acoustic impedance and are a powerful tool in studying small-scale acoustic scattering in biological tissue. 3DZMs are created from a series of adjacent histological images that have been aligned to one another to form a 3D volume. Each voxel of the reconstructed 3D volume is assigned a value of acoustic impedance. In the case of weakly scattering media, the 3DZM can be related to ultrasonic backscatter [2]. This is done through the use of intensity form factors which are scattering models for different scatterer geometries [3]. The form factor is related by the Fourier transform of the 3D spatial autocorrelation of the acoustic impedance distribution [7]. Equivalently the form factor can be computed as the squared magnitude of the 3D spatial Fourier transform, or power spectrum, of the impedance distribution due to the Wiener-Khintchine theorem [8]. Thus form factors are proportional to the power spectrum of an impedance distribution. This makes 3DZMs a very useful tool in studying small-scale acoustic scattering because they can provide a link between acoustic interrogation of tissue and histological evaluation, the latter being the current standard for diagnosis of tissue disease [9].

Chapter 2: Theory

2.1 Ultrasonic Scattering

Spatial variations in the density, ρ, and compressibility, κ, of a medium give rise to scattered ultrasound waves. Of particular interest is ultrasonic backscatter, which is the portion of the scattered wave that propagates in the opposite direction to the incident wave. The following development is based largely on the derivations found in [2, 7].

For a plane wave of unit amplitude incident on a weakly scattering volume, the far-field backscattered pressure is described by the spherical wave

$$p_{bs}(\boldsymbol{r}) = \frac{e^{-ikr}}{r}\Phi(2k)\ , \tag{2.1}$$

where $\boldsymbol{r}$ is the listener position and k is the acoustic wave number ($k = \frac{\omega}{c}$). The function $\Phi(2k)$ is the angle distribution function

$$\Phi(2k) = \frac{k^2}{4\pi}\iiint_{V_0}\gamma(\boldsymbol{r_0})e^{-2ikr_0}dV_0\ , \tag{2.2}$$

where V_0 is the scattering volume. The function $\gamma(\boldsymbol{r})$ is

$$\gamma(\boldsymbol{r}) = \gamma_\kappa(\boldsymbol{r}) - \gamma_\rho(\boldsymbol{r})\ , \tag{2.3}$$

such that the relative compressibility and density functions are defined as

$$\gamma_\kappa(\boldsymbol{r}) = \frac{\kappa(\boldsymbol{r}) - \kappa_0}{\kappa_0} \tag{2.4}$$

and

$$\gamma_\rho(\boldsymbol{r}) = \frac{\rho(\boldsymbol{r}) - \rho_0}{\rho(\boldsymbol{r})}\ , \tag{2.5}$$

where $\kappa(\boldsymbol{r})$ and $\rho(\boldsymbol{r})$ are the compressibility and density at position $\boldsymbol{r}$, and κ_0 and ρ_0 are the background compressibility and density, respectively. The backscattered intensity is then

$$I_{bs} = A|\Phi(2k)|^2. \tag{2.6}$$

In the case of weak scattering (γ_κ and γ_ρ are small) $\gamma(\boldsymbol{r})$ can be approximated as the first order Taylor series

$$\gamma(\boldsymbol{r}) \approx -2\frac{z(\boldsymbol{r}) - z_0}{z_0}\ , \tag{2.7}$$

where the impedance $z(\boldsymbol{r})$ and background impedance z_0 are defined, respectfully, as

$$z(\boldsymbol{r}) = \sqrt{\frac{\rho(\boldsymbol{r})}{\kappa(\boldsymbol{r})}}, \tag{2.8}$$

$$z_0 = \sqrt{\frac{\rho_0}{\kappa_0}}. \tag{2.9}$$

Combining Equations (2.2), (2.6), and (2.7) yields

$$I_{bs} = A' k^4 S(2k)\ , \tag{2.10}$$

where A' is a new proportionality constant and

$$S(2k) = \left| \iiint_{V_0} \frac{z(\boldsymbol{r_0}) - z_0}{z_0} e^{-2ikr_0} dV_0 \right|^2 \tag{2.11}$$

is the squared magnitude of the power spectrum of the relative impedance function. Modulo a constant, the power spectrum is seen to be related to the backscattered intensity divided by k^4. Thus it can be seen that if the impedance distribution of a volume is known, the backscattered ultrasonic intensity can be related to the power spectrum of the relative impedance distribution. This principle is the primary motivation for the use of 3DZMs in modeling ultrasound scattering in tissue.

2.2 Form Factors

Form factors are functions describing the backscattered intensity as a function of frequency for a particular scatterer geometry (spatial impedance distribution). Form factors are the ratio of the backscatter coefficient for a finite-sized scatterer to that of a point scatterer (Rayleigh scatterer). The backscatter coefficient of a point scatterer [7], given by Equation (2.12), is

$$\sigma_0 = \frac{k^4 V_s^2 \bar{n} \gamma_0^2}{16\pi^2}\ , \tag{2.12}$$

where V_s is the volume of the scatterer, $\bar{n}$ is the number density of scatterers, and $\gamma_0 = \frac{z - z_0}{z_0}$.

Hence the form factor $F(2k, d)$ can be related to the backscatter coefficient σ_b by

$$\sigma_b = \sigma_0 F(2k, d). \tag{2.13}$$

For discrete scatterers, the size d refers to the diameter of the scatterers whereas for continuously varying scatterers (such as Gaussian or exponential scatterers [7]) d is the effective correlation length.

In most cases, simple scatterer geometries having spherical symmetry (isotropic) are assumed, although a form factor can be calculated for any scattering configuration. The form factor is calculated as the Fourier transform of the spatial autocorrelation function of a medium containing a single scatterer, or equivalently as the squared magnitude of the Fourier transform of the medium (by use of the Wiener Khintchine theorem) [8]. At k = 0, the form factor is normalized to unity, and usually has a vanishing derivative. The form factor used in this thesis is known as the fluid-filled sphere form factor, which models a uniform fluid sphere embedded in a uniform background material. The fluid-filled sphere form factor is described by the equation

$$F(2k,d) = \left(\frac{3}{kd} j_1(kd)\right)^2, \tag{2.14}$$

where j_1 is the first order spherical Bessel function of the first kind. This form factor is plotted in Figure 2.1 for several different scatterer diameters.

As was previously stated, form factors are the squared magnitude of the impedance distribution of the scatterer. From Equation (2.11), it is clear that the power spectrum of a 3DZM will be proportional to an appropriate form factor. Thus by constructing the spatial impedance distribution of a sample of tissue, the ultrasonic backscattered power spectrum can then be calculated. The 3DZM can therefore be used to estimate tissue parameters such as ESD and EAC.

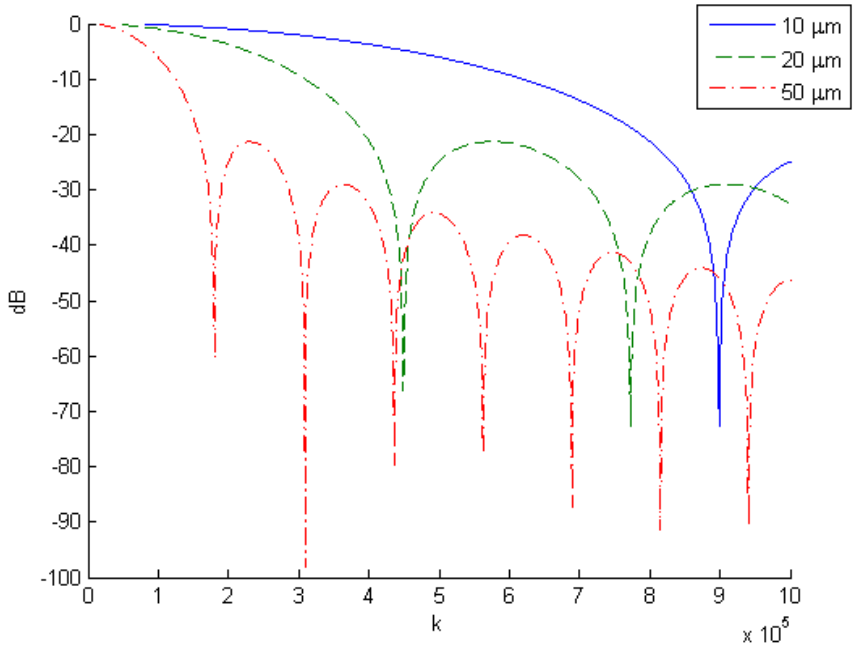

Figure 2.1: Fluid-filled sphere form factor for d = 10, 20, 50 µm.

Chapter 3: Map Construction

Three-dimensional impedance maps are computational phantoms constructed to mimic the scattering behavior of tissue. Each voxel of the computational volume represents the acoustic impedance of the tissue that is being modeled. The method was begun by Mamou [2] and continued by King [10] and Dapore [11]. The current work draws from all three of these sources. This chapter provides a summary of the current creation process of the 3DZMs, shown as a block diagram in Figure 3.1.

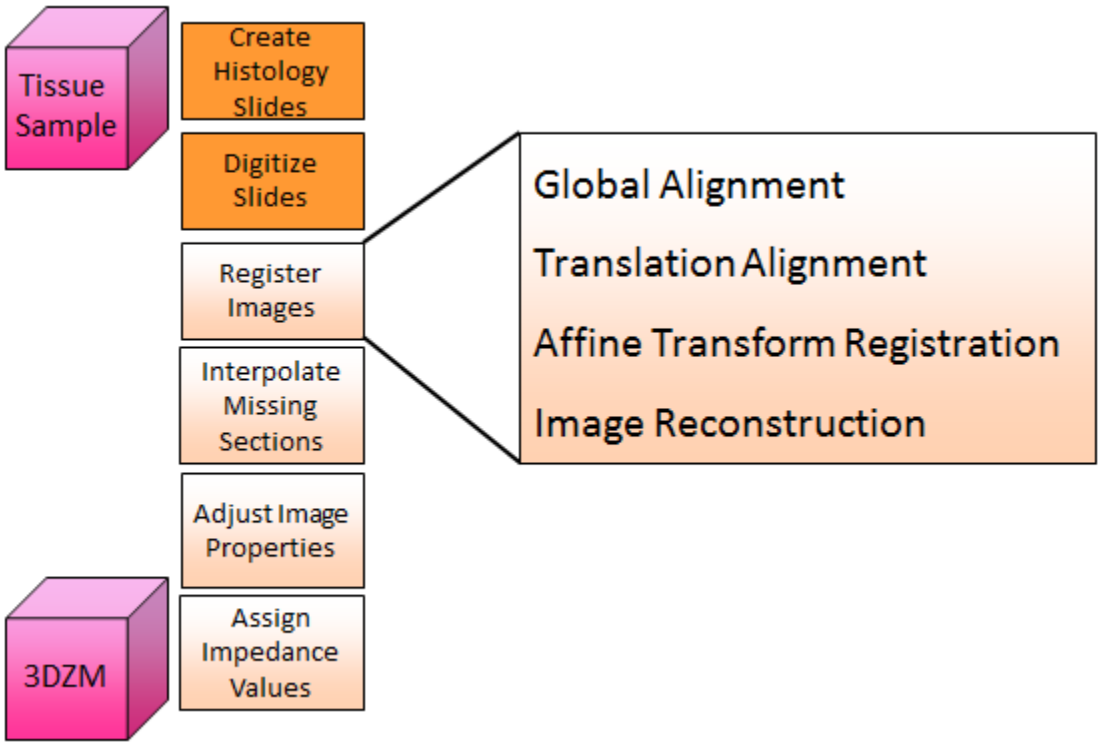

Figure 3.1: Block diagram of 3DZM creation process.

3.1 Histology Preparation and Digitization

The creation process begins by producing a set of serial histology slides of a sample of tissue. The sample is fixed in formalin, sliced into thin sections, stained with hematoxylin and eosin (H&E) and prepared as standard histology slides. The typical thickness of the slices is 3 µm, but

this is not required and thicker sections have been used. Increasing the slice thickness decreases the resolution of the 3DZM; however, there is sometimes a tradeoff between the slice thickness and the quality of the histology slide.

Each slide is digitized using a NanoZoomer HT slide scanner (Hamamatsu, Hamamatsu City, Japan) in 24-bit RGB color at a pixel resolution of 0.46 μm. A typical image has around 18,000 pixels to a side, or roughly 8000 μm.

3.2 Registration

During the histology preparation, the tissue sections undergo a certain amount of shrinking, stretching, and shearing, and are positioned on the slide in a variety of positions and orientations. Because of this, the images must be properly realigned with adjacent images in the series so that the resulting 3D volume is an accurate representation of the tissue from which it was created. This process is done with a computer registration scheme implemented in Matlab (The Mathworks, Natick, MA). Because of the high resolution (and hence the large file size) of the images, the registration is separated into stages in which the optimization of alignment is performed at different resolution levels. The final 3DZM that gets created represents a user-selected subsection of the entire tissue sample.

3.2.1 Global Alignment

The first stage, referred to as global alignment, is meant to give a rough alignment at the global level using highly decimated images. This stage allows for the use of the edges and white space of the images to find an approximate initial image transformation for the finer resolution stage.

Global alignment begins with two adjacent images that have been decimated so that their dimensions are close to 100 pixels. The images are then converted to gray scale and their backgrounds are artificially set to pure white to maximize correlation between the white space. Next, a search is performed to find an initial image translation (in the range of ± 25 pixels in both the x and y axes) using a minimum mean-squared error (MMSE) metric. Once this search has been performed, the best translation is applied to the second image and a search for the best

image rotation is performed using the correlation coefficient as a metric. For two adjacent images *I* and *J* of size M x N the correlation coefficient is calculated as

$$C(I,J) = \frac{\sum_{m=1}^{M}\sum_{n=1}^{N}(I_{mn}-\mu_I)(J_{mn}-\mu_J)}{\sigma_I\sigma_J}, \quad (3.1)$$

where μ and σ are the mean and standard deviation for the respective gray scale images. A narrow translation search is once again performed to make sure that rotation did not degrade the alignment of the tissue slices.

Using the values of rotation and translation found previously as the initial transformation, a Nelder-Mead simplex search [12] is performed to optimize the rigid set of transformations once again using the correlation coefficient as a metric. Obtaining as accurate a global registration as possible is important because of the degree to which the images have been decimated. A translation error of just one pixel amounts to a translation error of 200 or more pixels of the undecimated images.

As one final step, the correlation coefficient is examined to determine whether correlation of the images is sufficient. A substandard correlation usually results from tissue folding, tearing, or other irreversible changes of the tissue during the histology preparation. If correlation is found to be inadequate, the registered image is skipped and global registration is attempted with the next available image. Removing these images is a critical step in the 3DZM creation process because they often generate unacceptable registration parameters when proper alignment is not possible. This will cause discontinuities in the final 3DZM when it is constructed; therefore, these sections need to be removed and the missing data replaced with interpolated values at a later stage.

3.2.2 Fine Registration

The next stage is comprised of the steps labeled "Translation Alignment" and "Affine Transformation Registration" in Figure 3.1. After the proper global alignment transformations have been found and applied to two adjacent images, a dense search of translation parameters is performed on portions of the two images. These portions contain the user-selected subsection of the image for which a 3DZM is to be created at their center, as well as a margin of extra image information to improve robustness of the translation search. The image sections have also been

decimated to speed up the computation, although only by a factor of about 20, as opposed to the factor of several hundred in the global alignment stage. The metric for proper alignment is once again the correlation coefficient.

The final stage of registration attempts to find the full set of affine transformations, rotation, translation, stretching, and shearing. For this stage only the user-selected subsection of the large images is used, with no decimation applied. First, a set of 200 random rigid perturbations of the images is tested where the translation and rotation parameters are selected from a uniform random variable distribution ranging from -40 to 40 pixels and -10 to 10 degrees, respectively. From these trials, the set of parameters that result in the best mutual information [13] between images is chosen as the initial guess for rigid optimization using a Nelder-Mead simplex search. The optimization is also done using the mutual information metric. The mutual information for two images *J* and *K* is defined as

$$I(J,K) = \frac{H(J)+H(K)}{H(J,K)}, \tag{3.2}$$

where $H(J)$ is the entropy of image *J* and $H(J, K)$ is the joint entropy of images *J* and *K*. The entropy of an image is given by

$$H(J) = -\sum_j p_J(j)\log(p_J(j)), \tag{3.3}$$

where $p_J(j)$ is the probability of a pixel having the value *j* in image *J*. The joint entropy of two images is given by

$$H(J,K) = -\sum_j \sum_k p_{J,K}(j,k)\log(p_{J,K}(j,k)), \tag{3.4}$$

where $p_{J,K}(j, k)$ is the probability of a pixel having the value *j* in image *J* and *k* in image *K*.

After performing rigid optimization with the full amount of image data, these parameters are passed as an initial transformation for the full affine optimization stage. This is also a Nelder-Mead simplex search maximizing mutual information, this time over the entire six degrees of freedom (horizontal and vertical translation, rotation, horizontal and vertical stretching, and shear). Once this search is complete, the final set of transforms to be used in the 3D volume reconstruction has been found.

3.2.3 Reconstruction, Interpolation, and Intensity Normalization

Once the best set of image transformations has been found for each pair of adjacent images that will be used in the 3D volume, the cumulative set of transforms to each image is calculated. This

means that for an image in the stack, all the transformations found for the images leading up to it are applied in cascade to this image. With the entire stack of transformed images the volume can then be assembled.

At this point, any missing data due to missing or unusable slides is filled in with interpolated values. This is done so that each 2D image maintains its proper position in the 3D volume. Cubic Hermite interpolation is utilized for each vertical line of pixels through the volume and independently for the three color fields.

Each individual image must then be adjusted to correct for variations in brightness between images. Small differences in the slicing thickness of the tissue samples or differences in staining times will affect the amount of uptake of dye. By arguments made in [10], only the image saturation needs to be adjusted. The saturation is modified according to the equation

$$S_i' = (S_i - \mu_I)\frac{\sigma_{vol}}{\sigma_I} + \mu_{vol}\ , \tag{3.5}$$

where S_i' is the new pixel saturation, S_i is the original pixel saturation, and σ and μ are the mean and standard deviation of saturation. The subscript *I* refers to the mean and standard deviation of the image being normalized, and the subscript *vol* is of the entire 3D volume.

3.2.4 Impedance Value Assignment

The final stage of the 3DZM creation process is to assign acoustic impedance to each voxel based on its color value. Because it is very challenging to know precisely the impedance of each component of the tissue, instead a reasonable estimate is made. Assignments are made by relating the stain tissue color to elements of the tissue microstructure [2]. This is dependent on the dye with which the tissue is stained. As an example, for H&E stain tissue with a greater protein concentration appears pink, while tissue with a greater nucleic acid concentration appears blue. Any areas that appeared white are assumed to be fat.

To assign impedance, the 3D histology map (3DHM) is converted from RGB to the hue-saturation-value (HSV) color representation [14]. The general approach is to define a cutoff value in the hue to differentiate between the structures that have been stained different colors. Then a graded impedance is assigned based on the saturation of the pixel. Tables 3.1 and 3.2 show the general assignment scheme for H&E and Masson's trichrome stains.

Table 3.1: Impedance assignment values for H&E stain

Color	Tissue Structure	Impedance Range (Mrayl)
Light to Dark Pink	Cytoplasm	1.5 - 1.7
Light to Dark Blue	Cell Nuclei	1.8 - 2.0
White	Fat	1.45

Table 3.2: Impedance assignment values for Masson's trichrome stain

Color	Tissue Structure	Impedance Range
Blue	Collagen Fibers	1.75 - 1.80
Blue/Red/Pink mix	Muscle/Collagen mix	1.70
Red/Pink	Smooth Muscle	1.60 - 1.65
White	Saline	1.58

Chapter 4: Impedance Map Analysis

Through the developments in Chapter 2, it was shown that the squared magnitude of the spatial Fourier transform of a relative impedance function is proportional to a form factor model. Therefore by assuming a form factor model for the tissue, QUS parameters such as ESD and EAC can be calculated from the 3DZM. Additionally, the 3DZM can be examined in its initial form as a high resolution histology image, as well as segmented into high and low impedance structures to visualize in 3D. This chapter presents the power spectral estimation and QUS parameter estimation techniques for 3DZM analysis, along with a thorough test of the estimation process on simulated 3DZMs.

4.1 Power Spectral Estimation

Power spectral estimation is the process through which an estimate of the power spectrum of the 3DZM is obtained. The tissue medium is treated as a random medium, the 3DZM being a discretely sampled version of this medium. The power spectrum for an M-by-N-by-P 3D volume, a discrete version of Equation (2.11), is

$$F(k_x, k_y, k_z) = \frac{1}{MNP}\left|\sum_{x=0}^{M-1}\sum_{y=0}^{N-1}\sum_{z=0}^{P-1}\frac{z(x,y,z)-z_0}{z_0}e^{-2\pi i\left(\frac{k_x x}{M}+\frac{k_y y}{N}+\frac{k_z z}{P}\right)}\right|^2, \qquad (4.1)$$

where the acoustic wave number $k = \sqrt{k_x^2 + k_y^2 + k_z^2}$. While the components of k in the equation are technically indices, the true value for k_x (and analogously for k_y and k_z) can be found by multiplying by a factor of $\frac{\pi}{M \cdot dx}$ where dx (dy, dz) is the spatial sampling period in the x (y, z) direction. Equation (4.1) is implemented with a fast Fourier transform.

Coherent scattering arises from correlations between the positions of the scatterers in the medium; this effect is illustrated by Figure 4.1. One way to mitigate the effects of coherent scattering is to average over several radial paths through the scattering volume. In previous work this was done by fixing two of the k components in Equation 4.1 to zero and essentially computing an average 1D power spectrum for each of the three cardinal directions [10]. The three resulting power spectra were then averaged. However, using the entire 3D power spectrum utilizes all radial paths and is used in this work and in previous works [11].

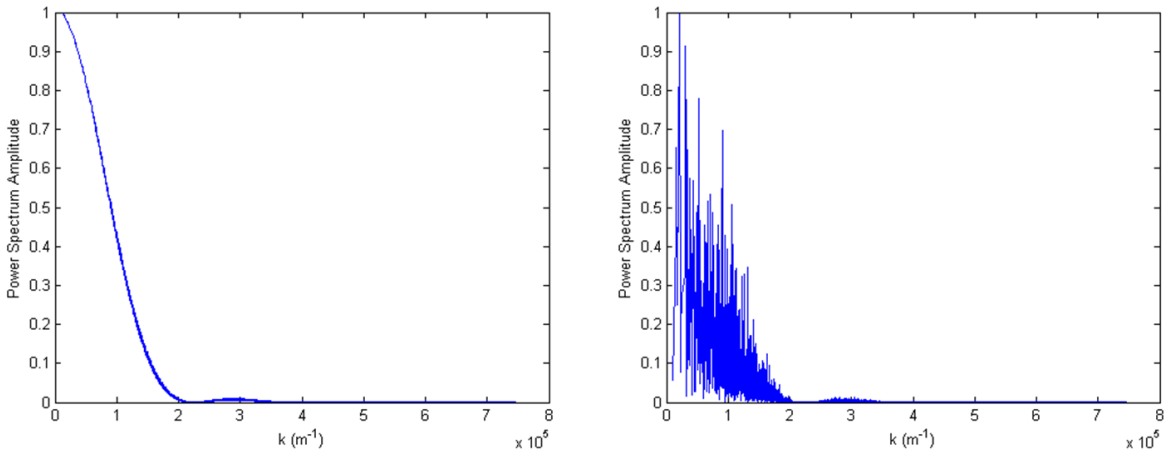

Figure 4.1: Power spectrum for a volume containing a single scatterer (a) and several scatterers (b). The effects of coherent scattering on the power spectrum are clearly present in (b).

4.2 Effective Scatter Diameter Estimation

In order to extract ESD estimates, the power spectrum is compared to the form factor model to find which scatterer size gives the best fit. Form factors with spherical symmetry (such as the fluid-filled sphere form factor used in this work) have a frequency dependence that scales based on the scatterer size only. An ESD estimate is produced by finding diameter *d* that satisfies

$$\hat{d} = \min_d \left(\sum_{k_x,k_y,k_z} w(k,d) \cdot \left| \log\left(S(k_x,k_y,k_z)\right) - \log(G \cdot F(k,d)) \right|^2 \right). \tag{4.2}$$

In this equation, *w* is a weighting term, *S* and *F* are the 3DZM power spectrum and theoretical form factor, respectively, and *G* is a normalizing gain parameter calculated as

$$G = \frac{\sum_k S(k) \cdot F(k)}{\sum_k (F(k))^2} = \frac{\langle S,F \rangle}{\langle F,F \rangle}. \tag{4.3}$$

There are many variations of Equations (4.2) and (4.3) that can be used as a means of fitting the theoretical and 3DZM form factors. In this work, the mean squared error of the base-10 logarithm of *S* and *F* was chosen as the error metric, and *G* was calculated in a manner which minimizes the mean squared error of *S* and *G*·*F*. Equation (4.2) also includes a weighting function which is dependent on both *k* and on the diameter being tested. This allows for a weighting towards different frequency bands in order to examine scatterers of different scale. Another type of weighting that has been used in the past is to enforce an optimal range of *k*·*a*

(where *a* is the scatterer radius), typically between the values of 0.5 and 2.0, since the form factors are most sensitive over this range [2].

4.3 Effective Acoustic Concentration Estimation

The effective acoustic concentration is a measure of the concentration and strength of scatterers and is equal to the quantity $\bar{n}\gamma_0^2$ from Equation (2.12). An estimate of the EAC from a 3DZM can be derived directly from the ESD estimate V_s as well as the gain parameter *G* (from Equation 4.2). The EAC is calculated as

$$C = \frac{G}{V_s^2} \tag{4.4}$$

and is often converted to the decibel scale by taking ten times the base-10 logarithm of *C*.

Chapter 5: Simulation

In order to test the accuracy and limitations of the ESD estimation process, a thorough set of simulations were run to assess the estimation for a variety of types of scattering volumes. These simulations tested the simplest cases of scattering as well as more unusual configurations like periodically located scatterers. The simulated 3DZMs were made to mirror the size and resolution of the typical 3DZMs created in practice in order for the comparison to be as close as possible.

5.1 Identical Spheres in a Uniform Background

The first set of simulations was identical spheres embedded in material of uniform background impedance. The size of the scatterers was varied from 6 to 70 μm between realizations to check for any size dependence in the estimation, and the concentration of scatterers was fixed so that the simulated volume contained 1% volume fraction of scatterers. Each realization was repeated ten times.

The ESD was estimated perfectly for all cases except for the case of the 6 μm scatterers in which the ESD was estimated to be 7 μm. The reason for this one case of error is possibly that as the size becomes small, it approaches the limit of resolution of the map in the *z* direction (which is the direction of slide alignment). It is likely that this diameter is the lower limit of sizes that can be accurately estimated from a 3DZM of this resolution.

More interesting were the results of the EAC estimation shown in Figure 5.1. The initial EAC measurements were in extreme error from the theoretical EAC values. However, when the bias in the estimates was removed, the estimated EAC matches almost identically to the theoretical values for each realization except, once again, in the case of 6 μm scatterers. However, the EAC estimate is dependent on the accurate estimation of ESD, so this error is not expected. Since the EAC is calculated on the logarithmic scale, the vertical offset of approximately 122 dB represents the scaling by a constant factor; in this case, the factor is 1.56e12. Thus it appears that the calculated power spectrum (Equation (4.1)) requires multiplication by a constant in order for it to be properly normalized.

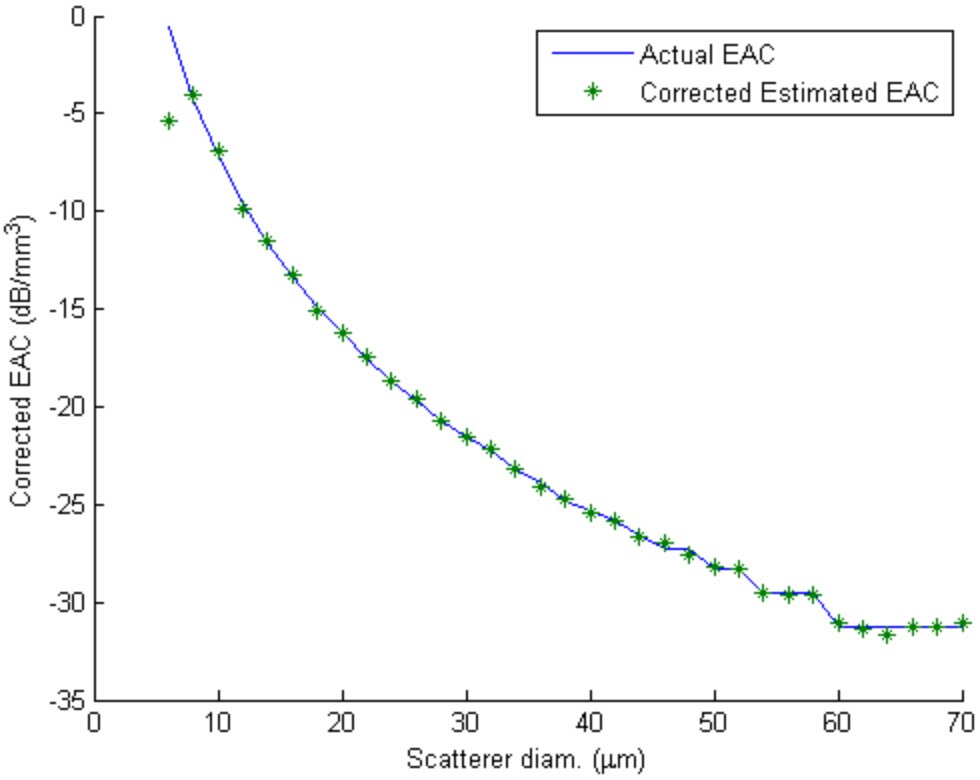

Figure 5.1: EAC results for simulated 3DZMs containing identical scatterers.

5.2 Identical Spheres Varying Concentration

The next set of simulations was designed to test whether the estimation was dependent on the concentration of scatterers. Volume fractions ranging from 5 to 25% in increments of 5% were tested with scatterer diameters ranging from 10 to 100 µm and each case was repeated ten times.

The ESD was estimated perfectly in all cases, so there was no effect of the concentration up to 25% volume fraction. Once again the EAC showed an offset between the actual and estimated values, shown in Figure 5.2. In this case, however, the offset was dependent on the scatterer concentration with the lower concentrations requiring a slightly greater offset than high concentrations.

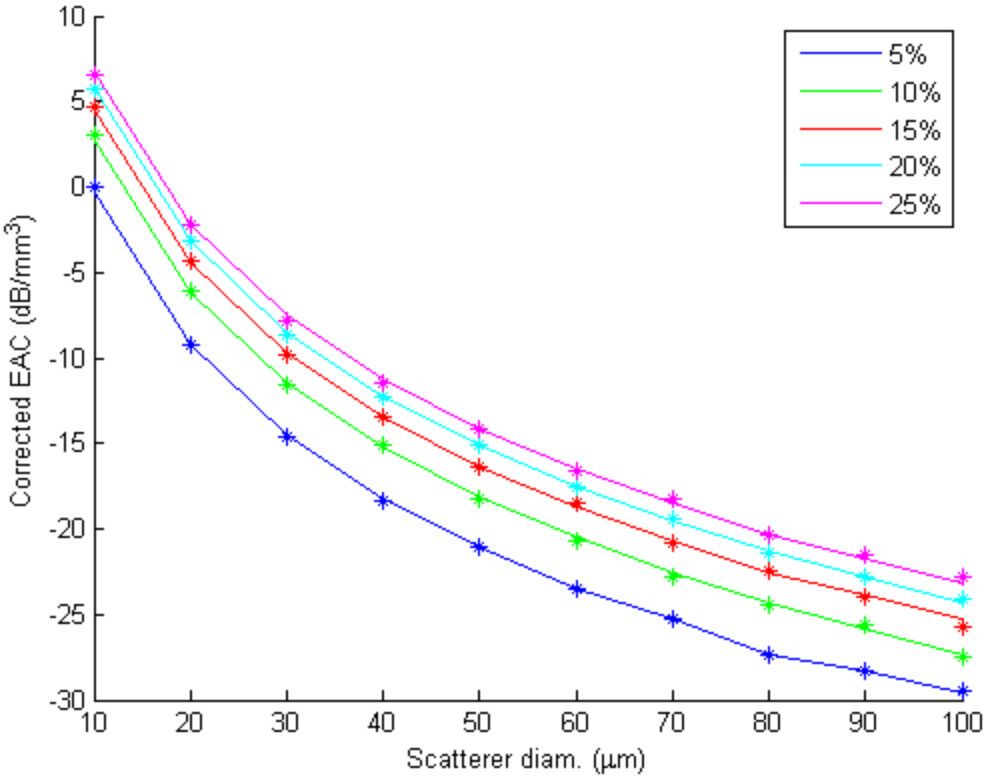

Figure 5.2: Offset corrected EAC results for simulated 3DZMs containing identical scatterers with different scatterer concentration.

5.3 Periodically Located Spheres

The effect of correlation between scatterer positions was tested by creating a set of maps in which the spherical scatterers are located at regular intervals in the volume. The scatterer size and spacing between scatterers was varied between realizations. Figure 5.3 illustrates that the ESD estimator was very inaccurate for small scatterer sizes with short distances between them. The accuracy generally improves with larger scatterer sizes and greater spacing, but this is likely due to the 3DZM containing very few scatterers, in some cases eight or only one. The inaccurate estimates are an expected result because one of the initial assumptions in the theory upon which the 3DZM method is based is that the location of the scatterers in the volume is random [7]. Because the EAC is dependent on estimating the ESD accurately, the EAC data was also highly inaccurate and the results are not included.

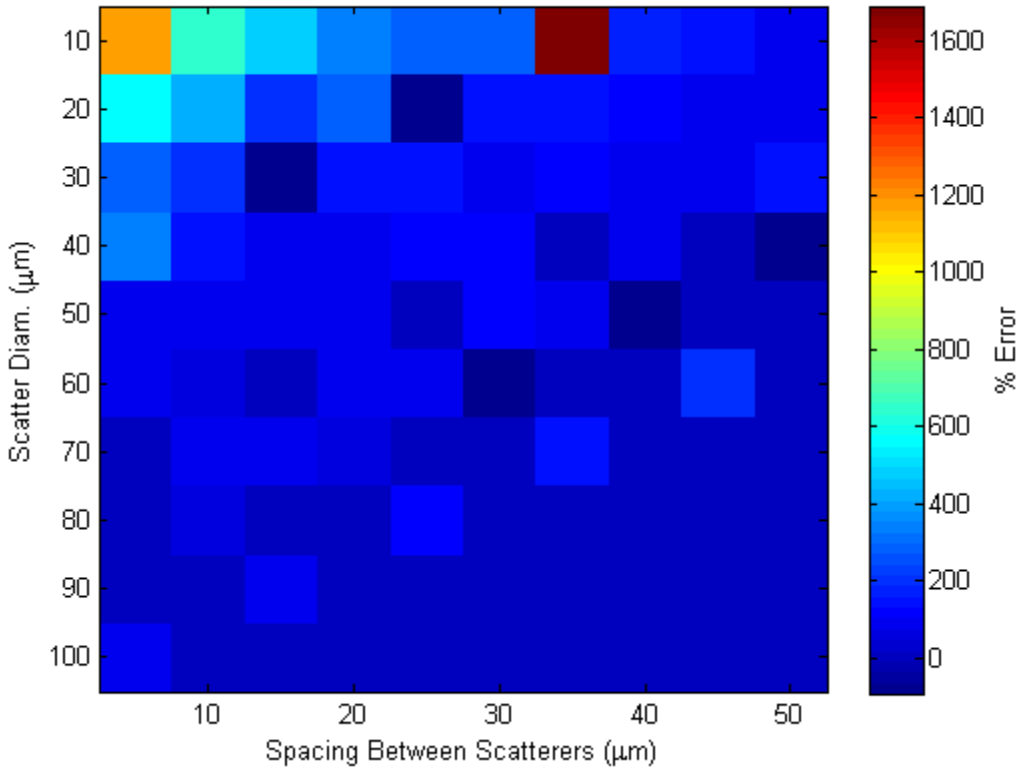

Figure 5.3: ESD results of periodically located spherical scatterers.

5.4 Identical Spheres with Random Noise

Finally, the effect of noise on the QUS parameter estimation process was tested. Various levels of noise were added to the 3DZM ranging from none to noise that could be up to twice the impedance difference between scatterers and background. The 3DZMs contained 20 µm scatterers at a volume fraction of 10%. Figure 5.4 shows that the ESD estimation was accurate until the noise level reached the scatterer impedance difference. The EAC estimates were also accurate up to this point when corrected for their offset.

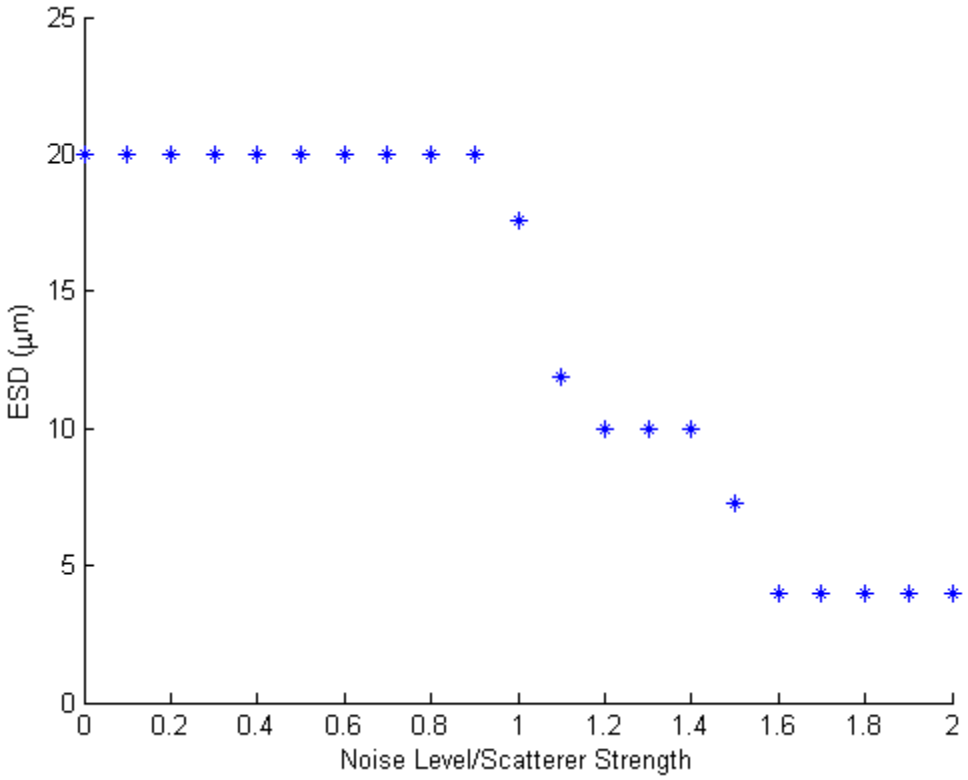

Figure 5.4: ESD estimates when different amounts of noise were added to the 3DZM.

Chapter 6: Tissue Studies

6.1 Rabbit Liver

Two samples of rabbit liver were analyzed using the 3DZM method. The first animal was fed on a high-cholesterol diet as part of a separate study and thus had fully developed fatty liver disease. The second rabbit had been fed on a normal high-fiber diet and had a normal liver. 24 3DZMs were created from each liver sample (for a total of 48) with dimensions 300 x 300 x 300 μm^3 (650 x 650 x 100 pixels). The regions of tissue for which 3DZMs were selected to be made were chosen to avoid blood vessels and any other higher-level structure. Histology images and 3DZMs of the two liver samples are shown in Figures 6.1 and 6.2, respectively.

Estimates of ESD were made for both rabbit liver samples with the fluid-filled sphere form factor and yielded average values of 7.5 ± 1.3 μm for normal liver and 7.0 ± 0.3 μm in fatty liver. This size corresponds fairly closely to a liver cell nucleus. The weighting function ($w(k,d)$ in Equation 4.2) for the estimation was chosen to give equal weights to all points of the computed 3D power spectrum. This, however, gives an implicit weighting towards smaller scatterer sizes because of the relatively large amount of points calculated at higher spatial frequencies than at lower spatial frequencies. Since the form factors are most sensitive in the range of 0.5 – 2.0 for $k \cdot a$ (and more available data points fall within this range when the radius a is small), the estimation tends towards smaller scatterer sizes. Given that the samples are mainly liver cells and nuclei without any other higher-level structure, this type of weighting is not unreasonable.

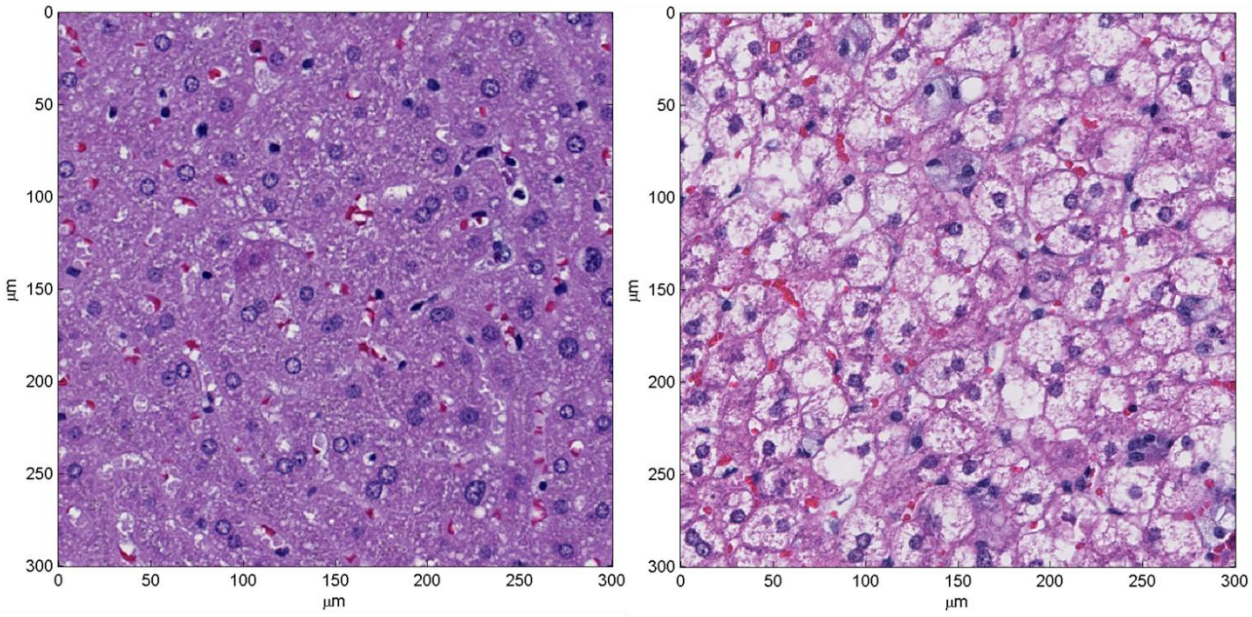

Figure 6.1: Histology images of (a) normal rabbit liver and (b) fatty rabbit liver.

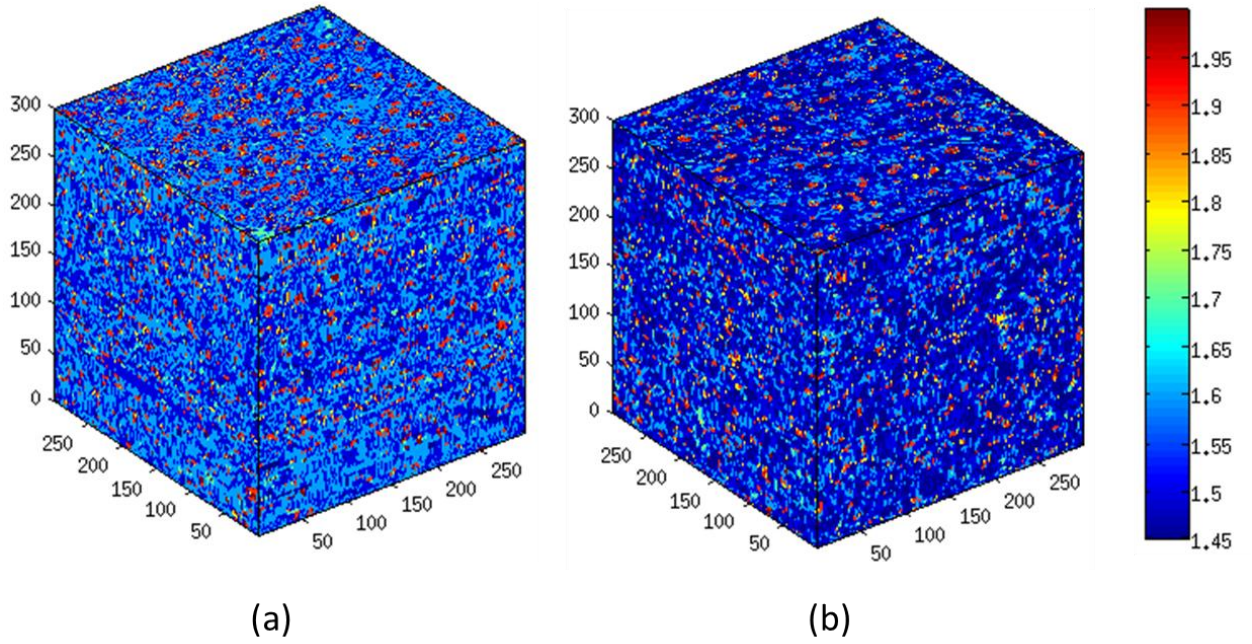

Figure 6.2: 3DZMs made from (a) normal rabbit liver and (b) fatty rabbit liver.

6.2 Rat Cervix

A sample of rat cervix was also analyzed. This sample was stained with Masson's trichrome rather than H&E. Seven 3DZMs were made from the sample, each with an approximate size of 300 x 300 x 100 μm^3. There are many different types of tissue layers in the cervix, but the location of the samples was chosen to be within areas mainly comprised of collagen fibers and smooth muscle tissue. Examples of histology images and the 3DZMs created from rat cervix are shown in Figures 6.3 and 6.4, respectively.

From the seven 3DZMs that were created from the cervical tissue, the average ESD was 11.3 ± 3.1 μm. It is difficult to tell from examining the histology images of the tissue what structure this size corresponds to. The cervical tissue chosen to make 3DZMs was mainly composed of collagen and muscle fibers which are not well modeled as fluid spheres. It could be more instructive to use a different scattering model, such as a cylindrical scattering model, that better approximates the geometry of the tissue. However, the fluid-filled sphere model was used because of a concurrent study of cervical tissue in which the ESD was being estimated from actual ultrasound data using this form factor. This allowed for a direct comparison of the 3DZM results to that of a live-animal ultrasound scan which was approximately 8.3 μm. While the estimates are not the same, the fact that they are close to one another provides further motivation for developing the 3DZM creation and analysis methods.

Another avenue of exploration would be to use a different stain for the histology preparation. The Masson's trichrome stain that was used in the preparation of this first set of slides is designed to highlight muscle and collagen fibers, as well as a third type of tissue (epithelium) which was largely ignored because it is not found in the region of interest for this tissue. It could be that different tissue structures which were not brought out by this type of dye are responsible for the ultrasonic scattering, and a different type of stain would be needed in order to see them in the histology images.

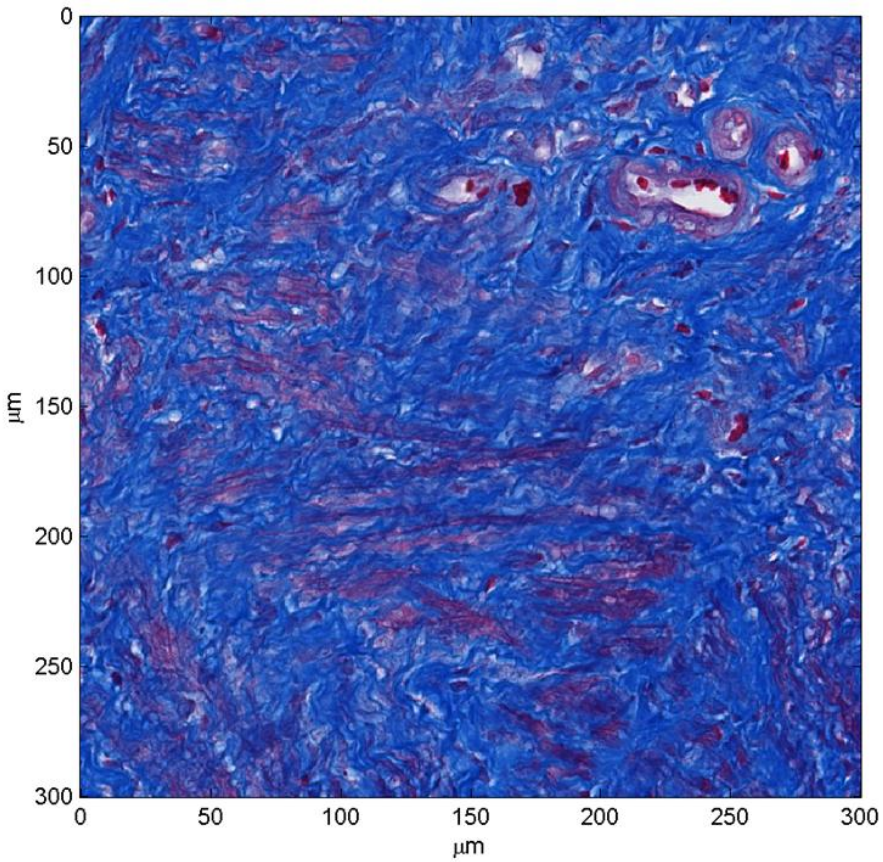

Figure 6.3: Histology image of rat cervix.

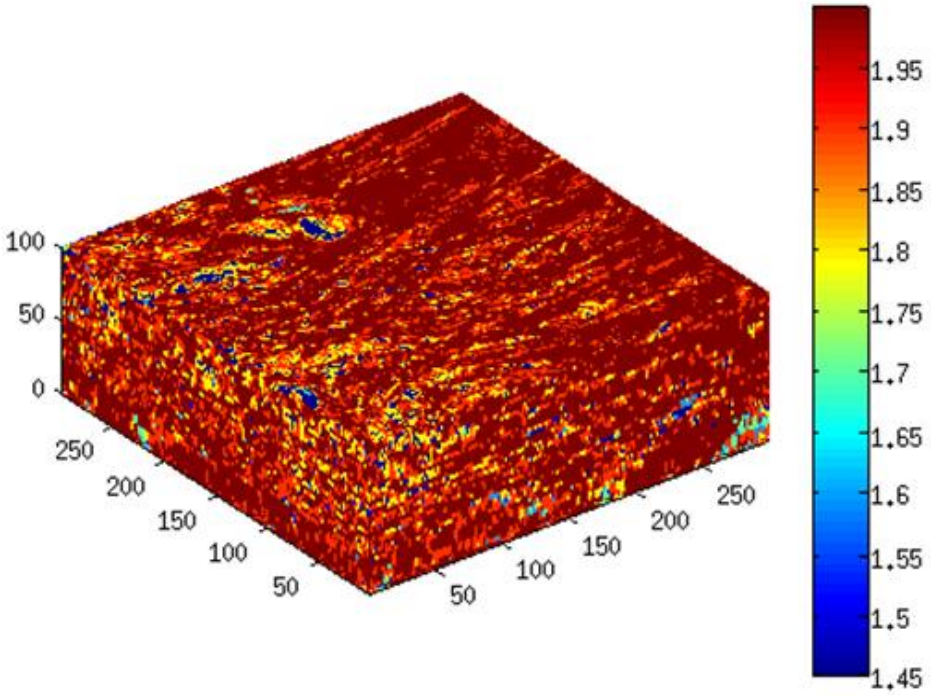

Figure 6.4: 3DZM of rat cervix.

Chapter 7: Conclusion and Future Work

The 3DZM method has shown itself to be a useful tool in the investigation of small scale acoustic scattering in tissue. In the case of liver, ESD estimates were close in size to that of an actual structure in the tissue, the nucleus. The ESD estimates from cervical tissue were reasonably close to estimates made from actual ultrasound data acquired from the same type of tissue. With continued improvements to the methods of map creation and analysis, more types of tissue can be studied to help elucidate what are the primary scattering sites in these tissues.

7.1 3DZM Creation

Excluding minor changes to the 3DZM creation routine, the main contribution of this author to the creation code was to restructure the registration stages so that they can be performed in parallel. The Matlab parallel computing toolbox allows for the global alignment, translation alignment, and affine registration stages to be performed on separate nodes of a computer cluster for each set of adjacent images that are being registered. These three stages represent the majority of the computation time in creating 3DZMs; hence, this improvement vastly speeds the creation process. Although computation time is of secondary importance to the quality of the image registration, the increased speed from the parallelization is a useful advantage that will allow for the creation of maps, particularly of larger size than have typically been created so far, in a reasonable amount of time.

7.2 3DZM Analysis

The 3DZM analysis routine was tested extensively with simulations of simple scattering volumes. It was seen through simulation that using the mean squared log error as a means of estimating the ESD was more accurate and precise than using the mean squared error as his been done in previous work. An EAC estimation has also been implemented which has results that are accurate relative to one another but are not absolutely accurate at this time. It is expected that once the correct normalization of the power spectrum is found the EAC estimator will also become absolutely accurate. The entire estimation routine has also been optimized for speed and

now provides the user with information regarding the fitting error, as well as a 1D visualization of the 3D power spectrum.

7.3 Future Direction

The breaking up of the 3DZM creation process into a multi-resolution scheme was a means to accurately and relatively quickly register the histology images to one another [9]. However, this process is not completely robust and incorrect registration still occurs, sometimes several times in the same 3DZM. These errors in registration likely cause problems for the QUS parameter estimation, although this has not been examined in great detail at present. A possible solution to the improper alignment is to further break down the creation process into more intermediate resolution stages. An added possibility is to register using all three of the pixel color fields, rather than operating only on gray scale versions of the images.

One other goal in refining the creation process is to produce considerably larger 3DZMs. The customary size of a 3DZM is typically a 300 μm cube. This size limits the accurate analysis of the 3DZM when trying to observe higher-level structure in tissue since most often a structure of size on the order of 100 μm will not fall entirely inside the 3D volume. Although there is a certain degree of user-control in the size and location from which to create maps, there are still many particulars in the creation coding which do not allow it to be scalable past a certain size of map. Further restructuring of the creation process would overcome these limitations and allow for the creation of larger maps.

The use of 3DZMs is not limited by the type of tissue that one wishes to examine. This thesis presents results for liver and cervical tissue. However, different types of tissue have been analyzed in the past, including fibroadenoma, carcinoma, and sarcoma tumors [15, 16]. Currently there are plans to use addition types of tumors, muscle tissue, and cell pellets [17].

There is also the possibility of comparing the 3DZM results of ESD and EAC with results obtained from actual ultrasound scans and subsequent QUS parameter estimation. Attempts had been made in the past to scan the fixed tissue sample before it was sliced for making histology slides, but it was later determined that comparing ultrasound scans of fixed tissue to 3DZMs that were meant to acoustically model live tissue was not an accurate comparison. However, it is certainly possible to ultrasonically scan live tissue before it is excised, fixed, and prepared for

histology, and this would be a much better comparison between ultrasound, histology, and 3DZM data.

References

[1] R. S. C. Cobbold, *Foundations of Biomedical Ultrasound* (Oxford University Press, New York, 1997).

[2] J. Mamou, "Ultrasonic characterization of three animal mammary tumors from three-dimensional acoustic tissue models," Ph.D. dissertation, Univ. Illinois Urbana-Champaign, Urbana, 2005.

[3] M. F. Insana, R. F. Wagner, D. G. Brown, and T. J. Hall, "Describing small-scale structure in random media using pulse-echo ultrasound," J. Acoust. Soc. Am. 87, 179–192, 1990.

[4] N. F. Maklad, J. Ophir, and V. Balsara, "Attenuation of ultrasound in normal liver and diffuse liver disease in vivo," Ultrasonic Imaging 6, 117-125, 1984.

[5] M. F. Insana, J.G. Wood, and T.J. Hall, "Identifying acoustic scattering sources in normal renal parenchyma in vivo by varying arterial and ureteral pressures," Ultrasound Med. Biol. 17, 613-626, 1991.

[6] B. L. McFarlin, W. D. O'Brien, M. L. Oelze, J. F. Zachary, and R. C. White-Trout, "Quantitative ultrasound assessment of the rat cervix," J. Ultrasound Med. 25, 1031–1040, 2006.

[7] M. F. Insana and D. G. Brown, "Acoustic scattering theory applied to soft biological tissues," in *Ultrasonic Scattering in Biological Tissues* (CRC, Boca Raton, FL, 1993), pp. 75–124.

[8] J. G. Proakis and D. G. Manolakis, *Digital Signal Processing* (Pearson Prentice Hall, Upper Saddle River, NJ, 2007).

[9] A. J. Dapore, M. R. King, J. Harter, S. Sarwate, M. L. Oelze, J. A. Zagzebski, M. N. Do, T. J. Hall, and W. D. O'Brien, Jr., "Analysis of human fibroadenomas using three-dimensional impedance maps," IEEE Trans. Med. Imag. 30 (6), 1206–1213, 2011.

[10] M. R. King, "Development and application of three-dimensional impedance maps related to tissue pathology," M.S. thesis, Univ. Illinois Urbana-Champaign, Urbana, 2007.

[11] A. J. Dapore, "Three-dimensional acoustic impedance map analysis of soft tissue," M.S. thesis, Univ. Illinois Urbana-Champaign, Urbana, 2010.

[12] J. C. Lagarias, J. A. Reeds, M. H. Wright, and P. E. Wright, "Convergence properties of the Nelder-Mead simplex method in low dimensions," SIAM Journal of Optimization, 9 (1), 112-147, 1998.

[13] J. V. Hajnal, D. L. G. Hill, and D. J. Hawkes, *Medical Image Registration* (Boca Raton, FL: CRC Press, 2001).

[14] G. H. Joblove and D. Greenberg, “Color spaces for computer graphics,” Comput. Graph. (ACM) 12 (3), 20-25, 1978.

[15] J. Mamou, M. L. Oelze, W. D. O’Brien, Jr., and J. F. Zachary, “Identifying ultrasonic scattering sites from three-dimensional impedance maps,” J. Acoust. Soc. Am. 117 (1), 413-23, Jan. 2005.

[16] J. Mamou, M. L. Oelze, W. D. O’Brien, Jr., and J. F. Zachary, “Extended three-dimensional impedance map methods for identifying ultrasonic scattering sites,” J. Acoust. Soc. Am. 123 (2), pp. 1195-1208, Feb. 2008.

[17] M. Teisseire, A. Han, R. Abuhabsah, J. P. Blue, Jr., S. Sarwate, and W. D. O’Brien, Jr., “Ultrasonic backscatter coefficient quantitative estimates from Chinese hamster ovary cell pellet biophantoms,” J. Acoust. Soc. Am. 128 (5), 3175-80, Nov. 2010.